Chemical Geology 615 (2023) 121217

Contents lists available at ScienceDirect

Chemical Geology

journal homepage: www.elsevier.com/locate/chemgeo

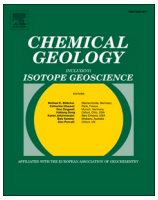

Degassed *versus* pristine: Evaluating melt inclusions with a new ATR-FPA-FTIR calibration and water imaging method in rhyolitic melts

Răzvan-Gabriel Popa [a,*], Peter Tollan [a,b], Jörg Hermann [b], Olivier Bachmann [a]

[a] Institute of Geochemistry and Petrology, ETH Zürich, Switzerland
[b] Institute of Geological Sciences, University of Bern, Switzerland

ARTICLE INFO

Keywords:
Melt inclusions
Dissolved water content
Water distribution
Eruptive styles
Degassing

ABSTRACT

The concentration of pre-eruptive volatiles is a key parameter that controls the eruptive behaviour of volcanoes. Among these, water is the most abundant volatile and has a major influence on magma chamber dynamics and a primary role in driving eruptions. While accurately quantifying the pre-eruptive dissolved water concentration of magmas is a crucial step in understanding eruptive styles, we still encounter problems in this regard. One of the main challenges is in discriminating pristine melt inclusions from those that lost water due to syneruptive and post-emplacement processes. To this end, we have calibrated a Fourier Transform Infrared (FTIR) setup with a Germanium crystal objective for Attenuated Total Reflectance analyses (ATR) coupled to a Focal-Plane Array detector (FPA), which allows the measurement of single-sided polished rhyolitic melt inclusions. The samples do not require any other special preparation routine, making it a versatile method (*i.e.* it can be applied to samples prepared for microprobe analysis). The setup generates high-resolution (4 μm) water distribution images that allow the quantification of dissolved water with an uncertainty of ±0.35 wt%. Water diffusion inside the melt inclusions can be identified on the spectral images, allowing for a qualitative analysis that, in most cases, can easily distinguish between pristine and degassed inclusions. We apply this setup to eight units (four explosive and four effusive) from the Nisyros-Yali volcanic center, in the South Aegean Sea, and compare the results with previously published hygrometry data. The results show that even in explosive units, which are generally considered unaffected by gas loss, up to 75% of the melt inclusions lost water. Because of this, the measured water contents show a spread over a range of ~2 wt%. Dissolved water contents in pristine melt inclusions match those from previous hygrometry calculations, indicating ~4 to 5 wt% H_2O. In effusive units, all the melt inclusions are degassed, yielding water contents that vary from 0 to 3.6 wt%, as compared to ~5.6 wt% H_2O given by mineral-melt hygrometry. The new setup and calibration provide a fast and cheap way for measuring water contents in calc-alkaline rhyolitic melt inclusions. Furthermore, our results indicate the importance of determining the pristine *versus* degassed nature of inclusions before any interpretations are made.

1. Introduction

Water is a major chemical component in most igneous systems, with key controls over the entire lifespan of a magma, from generation to storage and eruption. Whether in dissolved or exsolved state, this volatile affects many magmatic and volcanic properties and processes, including melt viscosity (Hess and Dingwell, 1996), the mobility of magmas (Pistone et al., 2013), magmatic differentiation through liquid segregation (Sisson and Bacon, 1999; Pistone et al., 2015), magma mixing (Degruyter et al., 2017), eruption styles and the explosive potential of a magma (Cassidy et al., 2018; Popa et al., 2021a; Popa et al., 2021b), eruption rates, duration and volumes (Huppert and Woods, 2002; Edmonds and Woods, 2018), and the mineralization of ore deposits (Sillitoe, 2010; Heinrich and Candela, 2014; Vigneresse et al., 2019). Despite being a critical parameter, water is elusive and challenging to determine in magmas due to its fugitive nature.

The most common methods of determining dissolved water contents in magmatic systems are the application of ***mineral-melt hygrometers***, like the calibration of crystal-liquid partitioning of albite and anorthite components by Waters and Lange (2015), and measurements of ***melt inclusions***, usually *via* infrared (IR) techniques (*e.g.* Wallace and Gerlach, 1994; Wallace et al., 1999; Bachmann et al., 2010; Wright et al.,

* Corresponding author.
E-mail address: razvan.popa@erdw.ethz.ch (R.-G. Popa).

https://doi.org/10.1016/j.chemgeo.2022.121217
Received 22 March 2022; Received in revised form 8 September 2022; Accepted 13 November 2022
Available online 18 November 2022

2012; Rangel et al., 2018; Tollan et al., 2019), Raman microspectroscopy (*e.g.* Thomas, 2000; Chabiron et al., 2004; Zajacs et al., 2005; Bachmann et al., 2010; Cassidy et al., 2016; Di Genova et al., 2017) and ion microprobe (*e.g.* Hervig et al., 1989; Deloule et al., 1995; Harms and Schmincke, 2000; Webster and Rebbert, 2001; Blundy and Cashman, 2005; Humphreys et al., 2008; Bachmann et al., 2010; Wright et al., 2012; Stock et al., 2018). The application of hygrometers is an indirect method, relying on assumptions of equilibria between minerals and melt, and on estimates of magmatic storage temperatures. This might easily yield erroneous results if the assessment of equilibrium is incorrect, or if the independent temperature determinations are faulty. The measurement of melt inclusions, on the other hand, is generally preferred over hygrometry as it is a direct approach. However, the results still depend on a key assumption, namely whether the melt inclusions retain the original records of water content, or whether they have lost water during eruptive and post-emplacement processes (diffusion-related degassing).

The commonly used criteria for determining the pristine or degassed quality of melt inclusions rely on physical and chemical examinations of the samples. Microscopic examinations of melt inclusions are employed to assess the presence of rupturing and of vapour bubbles, which are likely related to water loss (Bacon, 1992; Wallace et al., 1999; Wallace, 2005; Kent, 2008; Bachmann et al., 2010; Moore et al., 2015; Esposito et al., 2016; Donovan et al., 2018). However, the further complication of potential water loss by diffusion directly through the crystal host, without requiring rupturing, renders this method imperfect (Zhang et al., 1991; Severs et al., 2007; Portnyagin et al., 2008; Gaillard et al., 2003; Gaetani et al., 2012). An additional chemical criterion relies on comparing the dispersion in measured water contents to the behaviour of non-volatile elements, which could indicate whether significant degassing has occurred or not (Blundy and Cashman, 2005; Bachmann et al., 2010; Lloyd et al., 2013; Reubi et al., 2013). This method depends largely on the behaviour of the benchmarking elements, whose variation can be affected by other petrological processes, which are not accounted for (*i.e.* post-entrapment crystallization, mineral-melt boundary effects, recharge events). Overall, there is no direct approach for evaluating the quality of melt inclusions, which leads to ambiguity when interpreting large spreads in dissolved water contents. For example, it is challenging to discriminate whether observed variations are due to eruptive and post-emplacement gas loss (*e.g.* Portnyagin et al., 2008; Wright et al., 2012; Lloyd et al., 2013; Popa et al., 2019), or due to different storage pressures that reflect the vertical extent of a magmatic system (*e.g.* Bacon, 1992; Wallace et al., 1999; Wallace, 2005; Liu et al., 2006; Bachmann et al., 2010; Wright et al., 2012; Kilgour et al., 2013; Balcone-Boissard et al., 2018).

Another challenging aspect when working with melt inclusions is their small size, particularly when applying IR techniques. Traditional FTIR methods of analyzing water contents in melt inclusions rely on measuring the absorbance of the OH and molecular water stretching bands as the IR beam is transmitted through the glass (Stolper, 1982; Behrens and Nowak, 2003; McIntosh et al., 2014). This requires double-sided polished wafers of known thicknesses, which are time-consuming to produce, and difficult to prepare for small-sized inclusions (< 100 μm) without losing the material. The resolution of transmitted IR methods is also limited, and in many cases unable to resolve melt inclusions with diameters under ~30 μm (Devine et al., 1995).

A potential solution to quickly measuring the dissolved water content of melt inclusions regardless of size and without needing difficult sample preparation, is in applying ATR-FTIR spectroscopy, which was pioneered by Lowenstern and Pitcher (2013). ATR designates the use of an Attenuated Total Reflectance objective, which consists of a high refractive index crystal that comes in direct contact with the measured sample. The IR beam is transmitted through the ATR crystal and is totally reflected at the contact with the sample, where an evanescent wave is generated (Compton and Compton, 1993). The evanescent wave penetrates the sample to a depth dependent on the incidence angle of the IR beam and on the wavenumbers, but <1 μm for the wavenumbers of interest to determining water contents (Compton and Compton, 1993; Hammerli et al., 2021). The absorbance of the evanescent wave induces a near-surface signal in the mid-IR range that is then recovered by the detector. Lowenstern and Pitcher (2013) have also highlighted the possibility of the ATR-FTIR method to image variations of H_2O in melt inclusions, as it is potentially sensitive to small diffusion-related gradients in water. This was later shown to be a viable approach by combining the ATR objective with a Focal Plane Array detector (FPA), which can increase the spatial resolution of the measurements to 0.5 × 0.5 μm (Popa et al., 2019; Allabar et al., 2020; Allabar and Nowak, 2020).

The combination of ATR objective and FPA detector (ATR-FPA-FTIR spectroscopy) has been mostly employed to study organic compounds in pharmaceutical and biomedical research (*e.g.* Kazarian and Chan, 2006; Ewing et al., 2016). It was introduced for the qualitative petrological analysis of magmatic glasses by Popa et al. (2019) and for their quantitative analysis by Allabar and Nowak (2020), who calibrated their setup for analyzing volatile concentrations in experimental peralkaline rhyolites subjected to decompression-induced degassing. We have designed this new study with two main objectives. *First*, to propose an ATR-FPA-FTIR calibration for calc-alkaline rhyolitic glasses, complementary to the calibration for alkaline compositions of Allabar and Nowak (2020). *Second*, to explore the possibility of distinguishing between degassed and pristine melt inclusions based on water imaging, and to develop a direct approach to estimating the quality of melt inclusions.

We test our method and calibration on natural samples from eight eruptive units of the Nisyros-Yali volcanic center from the South Aegean Sea, which has been active over the past ~160 ky (Bachmann et al., 2019; Popa et al., 2020). We have selected these eight particular units (the Avlaki, Nikia, Post-caldera domes and Yali obsidian lava flows, and the Lower and Upper Pumices of Nisyros and Yali) because their pre-eruptive magmatic conditions are already well characterized (Popa et al., 2019; Popa et al., 2021b). Based on previous plagioclase-melt hygrometry calculations, the magmas generating the four explosive eruptions had between 4 and 5 wt% dissolved H_2O, and those leading to effusive activity had ~5.6 wt% dissolved H_2O (Popa et al., 2019). The difference in the results of the hygrometry is mostly due to colder storage temperatures prevailing prior to effusive events. In agreement with this, based on halogen behaviour in melt and apatite inclusions, it has been determined that the four effusive eruptions were generated by water-saturated magmas, which had a significant exsolved component during magmatic storage, while the explosive events involved magmas stored at water-undersaturated conditions (Popa et al., 2021b).

2. Methods

2.1. Sample preparation

We used unaltered rhyolitic samples from lava flows (4) and pumice deposits (4), erupted by Nisyros and Yali volcanoes in the past ~110 ky (Popa et al., 2020), namely the Avlaki and Nikia lava flows, the Post-caldera domes and the Yali obsidian flow, along with the Lower and Upper pumice deposits of Nisyros and Yali. To have comparable datasets, we analyzed the same rocks that were previously used in Popa et al. (2019, 2021b), when mineral-melt hygrometry estimates were performed, and we eliminated all visible enclaves at the start of the preparation process. The sampling locations can be found in the supplementary files.

Sample preparation involved detaching the crystals from the glass matrix using high voltage selective fragmentation (SELFRAG), followed by heavy-liquid mineral separation. Plagioclase and orthopyroxene crystals were hand-picked and mounted in epoxy resin, and subsequently ground with aluminum oxide paper and polished with a polycrystalline diamond suspension down to a grade of 0.25 μm.

The melt inclusions were selected for analysis based on BSE imaging using a JEOL JSM-6390 Electron Microscope. We selected orthopyroxene and plagioclase-hosted melt inclusions with regular geometric shapes, indicating inclusion by crystal growth rather than dissolution. Further analyses constituted FTIR spectroscopy of melt inclusions, for total water content and quality evaluation.

2.2. Calibration of ATR-FPA-FTIR spectroscopy

All FTIR spectroscopy was conducted at the Institute of Geological Sciences, University of Bern using a Bruker Tensor II FTIR attached to a Bruker Hyperion 3000 microscope. The spectrometer consists of a globar infrared source and KBr beamsplitter. The microscope houses two detectors (both liquid nitrogen-cooled): a Mercury Cadmium Telluride (MCT) detector for single point measurements with variable aperture size, and a Focal Plane Array (FPA) detector for infrared imaging. Both of these detectors were used in combination with either a 15× cassegrain objective, or an Attenuated Total Reflectance (ATR) objective with a Ge tip. All measurements were conducted in a sealed measurement chamber that was purged with dry air to minimize contamination from atmospheric volatiles.

The total H_2O concentrations of melt inclusions were determined by combining the ATR objective and FPA imaging detector (including low pass filter). ATR objectives generate sample absorbance by inducing total internal reflectance at the interface between the sample and the ATR element, resulting in an evanescent wave of infrared light that is transmitted through the uppermost portion of the sample. This brings the significant advantage of approximating "transmitted" IR light measurements of melt inclusions without the need to expose them on both sides. Furthermore, by combining ATR with FPA detector imaging, high spatial resolutions can be achieved (~0.5 μm) as the measured area is 32 by 32 μm and the FPA has 64 × 64 detector elements, permitting the measurement of inclusions that are too small for more routine infrared techniques (< 30 μm).

A major challenge with quantitative ATR-FTIR spectroscopy is the conversion of absorbance to H_2O concentration. Lowenstern and Pitcher (2013) conducted a comprehensive study of natural hydrous glasses in order to produce compositional-dependent calibrations for calculating H_2O concentrations from ATR-FTIR measurements. As highlighted by the authors, however, the calibration is dependent on the ATR element used, including the angle of incidence. Hence, the new calibration produced in our study is appropriate to the specific properties of the ATR element we used. Our calibration is based on three experimental hydrous rhyolitic glasses and on one anhydrous glass from the collection of ETH Zürich, covering a range from 0 to 5 wt% dissolved H_2O, of the following volatile-free composition: 79.5 wt% SiO_2, 11.6 wt% Al_2O_3, 4.3 wt% Na_2O, 4.6 wt% K_2O. These experimental glasses were produced in the same batch as HGG 0, 3, 4, 5 from Ardia et al., 2008, by direct fusion using a hot isostatic press, resulting in glass cylinders from where beads were subsequently cut.

To account for potential non-homogeneities in the water content distribution within each cylinder of reference material, the first stage of our work involved verifying the H_2O concentrations of the calibration glass beads we used, in comparison with those used by Ardia et al. (2008). This was achieved by standard transmission FTIR spectroscopy, combining the 15× cassegrain objective with the MCT detector. Ten measurements with a 50 × 50 μm square aperture were made on each glass fragment to establish reproducibility. H_2O concentrations were calculated from the absorbance of near-infrared bands located at ~5200 cm^{-1} and ~ 4500 cm^{-1} using a straight baseline drawn between ~5400–4800 cm^{-1} and 4660–4260 cm^{-1}. Note that a flexicurve baseline was also tried, and found to give indistinguishable results. Eq. 8 from Zhang et al. (1997) was used to convert the absorbance to H_2O concentration. For the nominally anhydrous glass, absorption centered at ~3550 cm^{-1} was used instead. Thicknesses of the glasses (0.7–1.3 mm) were determined using a Mitutoyo digital thickness gauge with a 200 μm diameter tip for precise placement. We observed that the experimental hydrous glasses were saturated in a gas phase and contained bubbles. Raman spectroscopy measurements performed on a sealed bubble just beneath the glass surface indicates that the gas phase is dominated by CO_2 and N_2, and does not contain detectable amounts of molecular H_2O (Fig. 1). Under these conditions, the bubbles are expected to influence the measurements of the water content, by affecting the bulk absorbance of the IR beam as it passes through the calibration standards. To obtain a more precise H_2O estimate, the volume contribution from these bubbles was calculated. This was achieved by making reflected light measurements of the glass surface and then calculating the ratio of bubble to glass using the software Image J (Schneider et al., 2012). This resulted in a correction of 6% to the total thickness, which (as seen below) yielded water contents closer to those of Ardia et al. (2008).

The second stage involved determining the water band absorbance of the calibration glasses using the ATR objective coupled with the FPA detector. The ATR objective comprises a two-reflection ATR element composed of Ge (refractive index = 4.0), with internal and external incidence angles of 21.5° and 37°. Samples were placed beneath the ATR objective in a sealed chamber (with dry air purging), and an image map of the analysis area was made using the automated FPA Wizard tool of the OPUS software provided by Bruker. The ATR objective was then set into analysis position (pressure setting of "2", equivalent to 2.6 N of force), and the entire system left for 5–10 min to ensure that both moisture and air turbulence within the chamber were minimized. A background through air was taken, and the sample measured immediately afterwards by bringing the sample surface into contact with the ATR objective. Both background and sample measurements were fully automated, allowing the sample chamber to remain closed, ensuring consistent atmospheric conditions during this procedure. The sample chamber, however, had to be opened before manually selecting new analyses positions. The analyses were conducted with 128 scans at a wavenumber resolution of 8 cm^{-1} over the infrared wavenumber range of 900–3850 cm^{-1}. The FPA detector acquires 4096 spectra simultaneously over a square grid with the approximate dimensions of 32 × 32 μm, giving a raw pixel resolution of ~0.5 × 0.5 μm. In order to improve data quality, 8 × 8 pixels were binned together after data acquisition to give a final resolution of ~4 × 4 μm. A linear baseline between wavenumbers 2700 cm^{-1} and 3700 cm^{-1} was drawn, and the linear absorbance of the H_2O band centered at ~3500 cm^{-1} was calculated (Fig. 2 A, B). This was then combined with the H_2O measurements performed at

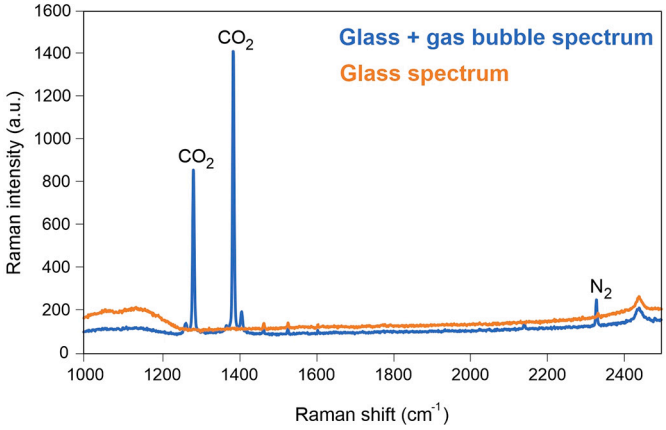

Fig. 1. Raman spectroscopy measurement on the calibration materials, showing the combined signal of glass and entrapped gas bubble (blue), compared to a pure glass signal (orange). The gas bubbles found in the rhyolitic standards are dominated by CO_2 and N_2, with no detectable amounts of molecular H_2O. (For interpretation of the references to colour in this figure legend, the reader is referred to the web version of this article.)

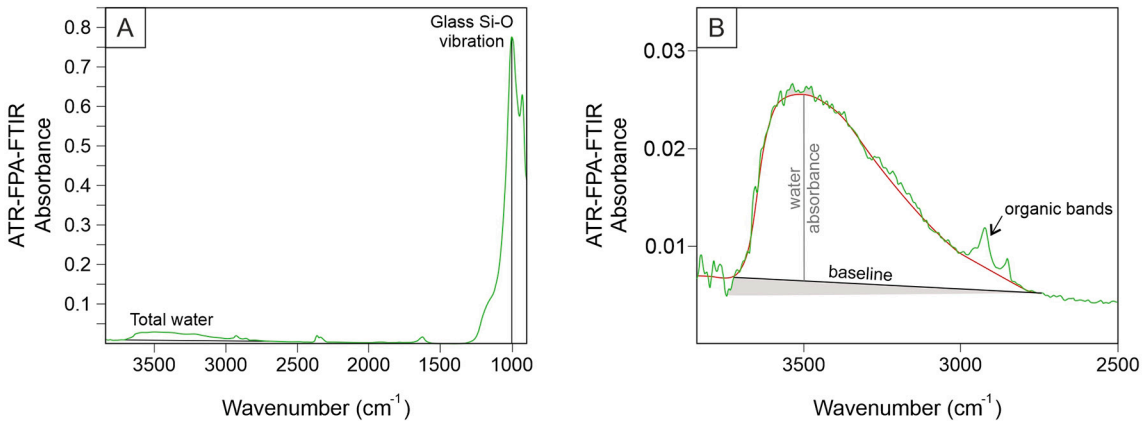

Fig. 2. Example of an IR spectrum of melt inclusions acquired with the ATR-FPA setup, from the Lower Yali pumice unit. (A) shows the overall shape of a spectrum, including the total water and glass Si—O vibration bands used for generating the absorbance images and for evaluating the dissolved water contents. The smaller peak immediately right of the glass signal represents the Si—O vibration band of the crystalline host. The linear absorbance is measured relative to the baselines, based on peak height (vertical lines). (B) is a close-up of the spectrum over the wavelengths specific to the total water signal, showing the effect of noise caused by atmospheric humidity and air turbulence within the measuring chamber. Here, the baseline and the water absorbance peak are set manually, so their positions reflect the reconstructed, smoothed spectrum. The areas marked with grey would normally be included in the absorbance estimate by the automated procedure. This can lead to an overestimation of the dissolved water content of ~10% relative. The organic bands can negatively affect the quality of the water distribution maps if they are high in intensity, but are eliminated during data processing in the OPUS software by the straight line generation function.

step 1, resulting in the calibration line that is presented in the results section.

2.3. ATR-FPA-FTIR measurements of melt inclusions

The ATR measurements of the natural melt inclusions were performed and processed similarly to the standards. When the melt inclusions were larger than 30 μm, we used a combination of multiple square grids. After data acquisition and binning, we corrected potential spectra anomalies (induced by epoxy resin) that were observed to appear roughly between wavenumbers 2700 cm^{-1} and 3000 cm^{-1} (Fig. 2 A, B) by generating a straight line over this frequency range. Afterwards, we computed the equivalent to total H_2O by calculating the absorbance at ~3500 cm^{-1} for all the measurement points contained in a grid (using the linear absorbance at the peak, *i.e.* signal intensity). The baseline anchor points between wavenumbers 2700 cm^{-1} and 3700 cm^{-1} were adjusted manually for each measurement to ensure that noise in the spectra did not inadvertently contribute to an inaccurate H_2O content (Fig. 2 B). The final total water absorbance images were generated using the data interpolation routine of the OPUS software. These absorbance values were subsequently converted to total H_2O using the calibration described in the results section.

Similarly to the water distribution, we imaged the overall structure (size and shape) of the melt inclusions (Fig. 3) using the Si—O vibration band of the glass at ~1020 cm^{-1} (Fig. 2 A). This is expected to give an overall assessment of the quality of the analysis. A good quality measurement needs the ATR objective to be in proper contact with the sample (Lowenstern and Pitcher, 2013): no surface irregularities on the sample, no sample movement and no sample breakage during the measurement due to the pressure exerted by the ATR objective. If the ATR-sample contact is good, the Si—O vibration image (referred to as 'structural imaging' henceforth) will successfully reproduce the shape of the melt inclusion as it appears in other types of imaging, such as back-scattered electron, secondary electron or optical reflection microscope images. Additionally, the structural imaging of the glass provides a baseline for comparison with the water distribution images, which as discussed later, is a key aspect to interpreting the state of the melt inclusions (degassed or pristine).

It is important to mention that the binning of the detector elements, although reducing spatial resolution, is essential to generating interpretable water distribution images. The main challenge that this

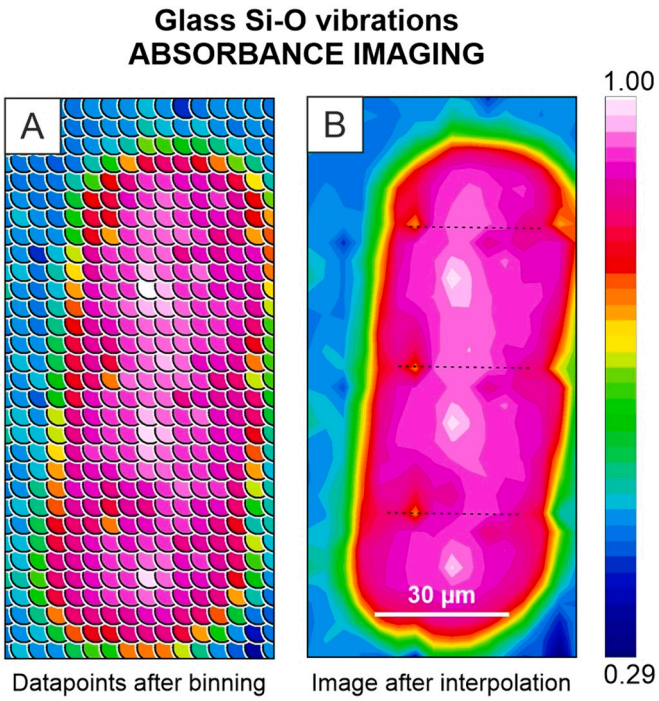

Fig. 3. Example of generating a spectral image, in this case for the glass Si—O vibrations of a pyroxene-hosted melt inclusion from the Lower Pumice unit of Nisyros volcano. Each individual data point that resulted after binning (A) contains a spectrum. The absorbance values are then interpolated using the OPUS software to generate the total water and structural absorbance images (B). In this specific case, the melt inclusion was analyzed by combining 8 square grids of 32 × 32 μm each. Note that at the contact areas between the grids (the edges of the ATR objective) the images show artifacts probably resulted from imperfect objective-sample contact (indicated with dashed black lines).

procedure overcomes is the low signal-to-noise ratio that becomes apparent at the low absorbance intensities characteristic for the total water band (Fig. 4 A). The noise is reduced through the binning process, which improves the quality of the spectra, emphasizing the gradients in water distribution (Fig. 4 B).

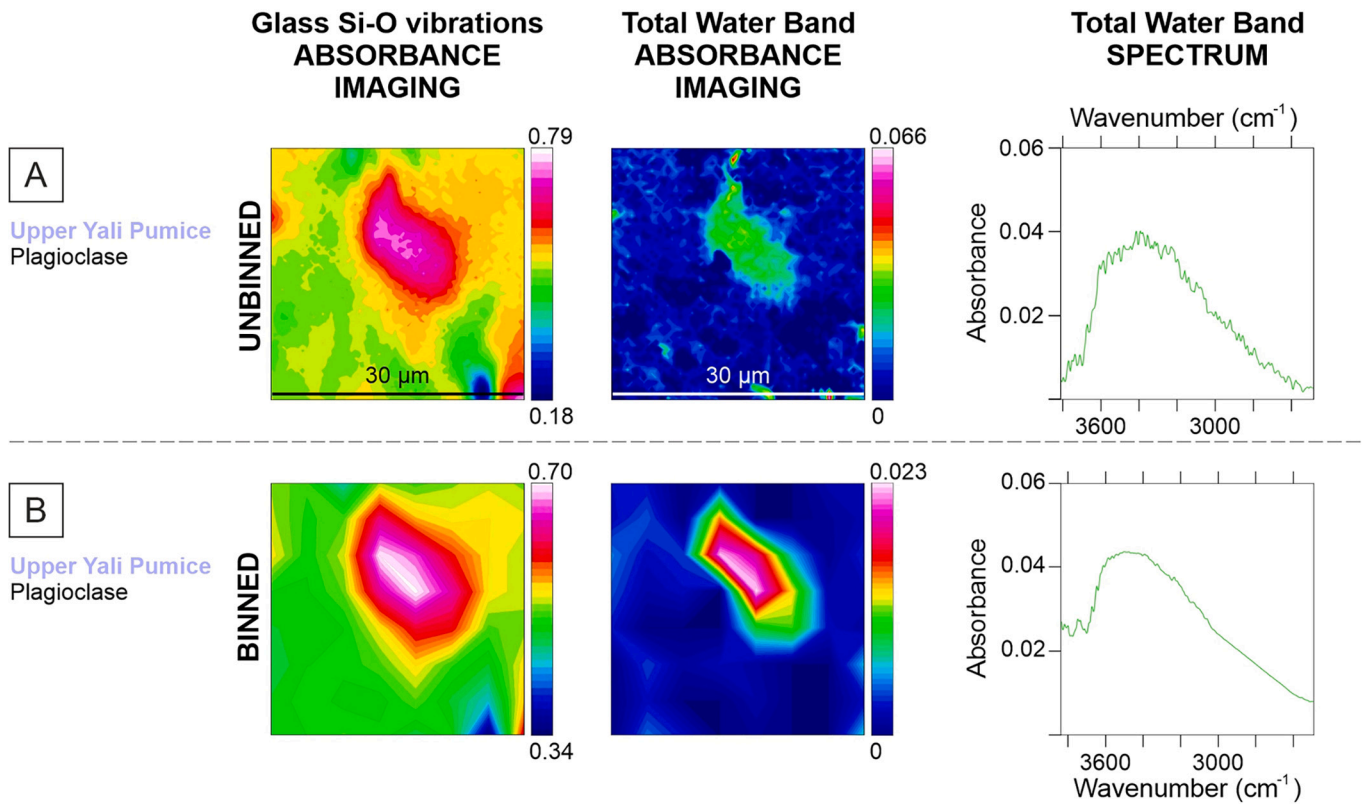

Fig. 4. Spectral imaging for the same melt inclusion, with detector element binning not applied (A) and applied (B) during the data processing routine. Although the glass Si—O vibration images are comparable between the two examples, the binning procedure makes a significant difference in the case of the water distribution images, reducing the noise and improving the quality of the spectra.

Standard measurements on calibration glasses were run regularly throughout the measurement sessions, to check for reproducibility and accuracy. The results of the analyses are given in the electronic supplementary material.

3. Results

3.1. Calibration equation for H_2O content by ATR-FPA-FTIR

Based on transmitted infrared light measurements, the resulting H_2O contents for the four rhyolitic calibration glasses are 0.03 wt%, 2.1 ± 0.1 wt%, 3.0 ± 0.1 wt% and 4.9 ± 0.1 wt%. Applying the correction to account for voids formed during bubble growth results in an increase in the calculated H_2O contents for the three water-bearing glasses, to 2.3 ± 0.1 wt%, 3.2 ± 0.1 wt% and 5.2 ± 0.1 wt%, respectively. These values are taken as reference for the calibration of the ATR-FPA.

The ATR-FPA dataset consists of repeated measurements of the calibration glasses over multiple analytical sessions, the entirety of which were used for the calculations of average absorbance and standard deviation. The calculated uncertainties thus take into account day-to-day variation in the performance of the detector/objective, the heterogeneity of the calibration glasses and the heterogeneity of the detector elements. The results of the calibration are presented in Fig. 5. A linear least squares regression of the data results in the following equation for calculating the total dissolved H_2O:

$$H_2O_{total}\ (wt\%) = 263 \times A – 0.9$$

Where A is the maximum absorbance of the band centered at ~3500 cm^{-1}, measured by ATR-FPA. Uncertainty on the regression is equivalent to ±0.35 wt% H_2O. Limit of detection is estimated at ~0.5 wt%. This equation is subsequently used for calculating the H_2O concentrations of mineral-hosted melt inclusions, as presented below.

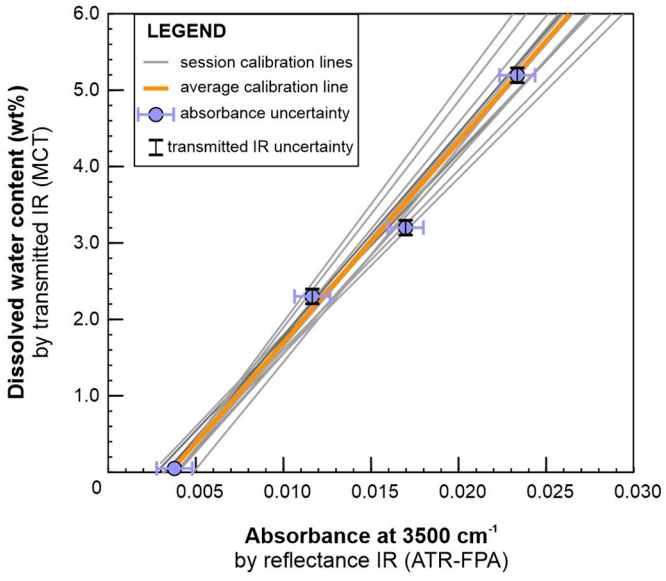

Fig. 5. The ATR-FPA calibration line (orange) for hydrous rhyolitic calc-alkaline glasses, which can be used to estimate the dissolved water content of rhyolitic melt inclusions. The session-dependent calibration lines are also depicted in grey. For estimating the water contents in melt inclusions we use the global regression (orange).

Using the water content evaluations from Ardia et al. (2008) for the standard glasses, changes the coefficients of the calibration equation from 263 to 258 (a) and from −0.9 to −0.7 (b). This induces water content differences of around 0.15 wt% for melt inclusions having >4 wt

% dissolved water, and of about 0.2 wt% for those having <2.5 wt% dissolved water.

3.2. Total water content imaging

When comparing the water absorbance and structural imaging of the melt inclusions, we generally observe four trends. *First*, the water content and glass structure images appear similar, showing comparable gradients in absorbance, with the maximum water and glass Si—O vibration signals coinciding (Fig. 6 A, B). We refer to this as *homogenous water distribution*. *Second*, we observe shifts between the maxima of the glass and total water absorbance, which in this case correspond to different areas of the inclusions (Fig. 6 C, D). *Third*, the water content is distributed irregularly within the inclusion, appearing 'shaggy' with no or little correlation to the gradients generated by the glass structure (Fig. 6 E, F). We refer to these last two trends as *inhomogeneous water distribution*. *Fourth*, although the glass structure has a clear signal, the total water absorbance is below detection limit, and in our case indistinguishable from that of the surrounding crystal (Fig. 6 G).

When looking at the ratios of the total water to glass Si—O vibration absorbance (Fig. 6, fourth column), we observe that it increases within the melt inclusions that have homogenous water distribution (A, B). This is due to a sharper increase in the intensity of the total water absorbance compared to that of the glass. The ratios flatten out and show spiky irregularities when the water distribution is inhomogeneous, indicating that the positive correlation between the two types of absorbances is not perfectly satisfied (D—F). In the last case, where the total water absorbance is below detection limit, the ratio decreases, showing a negative anomaly (G).

3.3. Water content estimates in Nisyros-Yali melt inclusions

In explosive units, between 25 and 80% of the melt inclusions have homogenous water distribution (Fig. 7, blue solid symbols). Notably, in the caldera-forming deposits of Nisyros only 25–35% of them can be classified as homogenous, while in the smaller and submarine explosive events of Yali, they make up 65 to 80% of the analyzed melt inclusions. Overall, melt inclusions with homogenous water distribution show variations in dissolved water content on the order of 1 to 1.35 wt% between minimum and maximum values, up to maximum dissolved water contents of ~5 wt%. These fit well within uncertainty of the hygrometry-derived value (Fig. 7, hygrometry values from Popa et al., 2019). The minimum water contents are generally between 4.1 and 3.6 wt%.

The melt inclusions with inhomogeneous water distributions (Fig. 7, blue open symbols) show higher variations in measured water contents for the caldera-forming eruptions of Nisyros, of the order of 1.35–1.7 wt %, and relatively lower differences for the smaller-scale explosive events of Yali, of 0.5–0.95 wt%. The maximum and minimum water contents are always lower than the inclusions having homogenous water distribution. They range from approximately 4.5–2.8 wt% for Nisyros, and 4.2–3.2 wt% for Yali.

In effusive units, all the melt inclusions show inhomogeneous water distribution (Fig. 7, red symbols). The dissolved water contents vary from detection limit up to maximum values of 3.3–3.6 wt%, and are significantly lower than the hygrometry-derived values of ~5.6 wt% dissolved water.

There is generally an overlap in the dissolved water contents measured in melt inclusions trapped by plagioclase and orthopyroxene.

4. Discussion

4.1. Technical developments

One of the key features of the ATR-FPA-FTIR setup is the ability to image both the structure and the water distribution of a melt inclusion. When comparing the two types of images, we consistently identify the four trends described above, which we classify as homogenous and inhomogeneous water distribution. This information can be used to estimate the pristine or degassed quality of the melt inclusions.

Overall, the total water image can indicate water loss from a melt inclusion, but this requires a careful examination of both water and structural images. IR imaging based on the absorbance of the evanescent wave is a diffusive method, and hence the maximum absorbances, both for the total water and for the Si—O vibrations of the glass are expected to occur near the center of the inclusion, farthest from the crystal host. Consequently, the absorbance values are expected to decrease towards the margins, where the crystalline structure of the host mineral locally affects the absorbance of the IR evanescent wave (Fig. 6). This effect is potentially enhanced by the actual sample penetration depth of the IR beam, which in certain cases has been shown to be up to 2–3 times deeper than the theoretical value of 1 μm (Mirabella, 1983; Kazarian and Chan, 2013). This leads to the quasi-concentric absorbance distribution observed in both water and structural images. However, depending on the shape of the melt inclusion and on the angle and thickness at which it is exposed, the location of the maximum might vary from measurement to measurement. This could also be influenced by gradients observed in the structural image, resulting from contact between the sample and the ATR objective (crystal breakage during measurement, sample imperfections due to grinding and polishing, fractures) (Lowenstern and Pitcher, 2013), or to fluid or mineral inclusions. Overall, having taken all these into account, for a pristine melt inclusion the total water image should display similar gradients to the structural image. Additionally, we note that the strongest glass Si—O vibration signals correspond to areas where the ATR-sample contact is best and where the crystalline host affects the signal less, or not at all. Therefore, the same areas of the melt inclusion are also expected to display the strongest water absorbance signal (Lowenstern and Pitcher, 2013). This is the case observed for the first trend described from our dataset, where the water images resemble the structural images, and the maximum absorbance of water and Si—O glass vibrations correspond. We interpret the melt inclusions with homogenous water distributions as being pristine and unaffected by significant water loss.

Accordingly, deviations from this trend depend on gradients in dissolved water content, due to diffusion or degassing. This could lead to the shifts between the location of the maximum total water and maximum Si—O glass absorbance signals, and to water images that deviate from structural images in size, shape and/or absorbance gradients. Consequently, the ratios of total water to glass Si—O vibration absorbance display an irregular trend, the positive correlation that is inherent to them not satisfied anymore due to water movement within and outside the melt inclusions. Hence, what we refer to as inhomogeneous water distribution can be interpreted as a result of partial water loss due to diffusion.

To test this, we performed ATR-FPA-FTIR measurements on the same melt inclusion, before and after being exposed to a microprobe electron beam (Fig. 8), which is known to induce element diffusion in sensitive materials such as glasses (Devine et al., 1995; Morgan and London, 1996; Humphreys et al., 2006; Allaz et al., 2019). The electron beam was set to a voltage of 15 kV, 2 nA current, it was defocused to 5 μm and the total exposure time was 80 s. Prior to beam exposure, the structural and water content images appeared similar, yielding a homogenous water distribution based on which the quality of the melt inclusion is interpreted as pristine. After electron beam exposure, the water content within the melt inclusion reorganized, migrating from the center and lower regions (which were affected by the microprobe) to the upper rim (Fig. 8). This illustrates the sensitivity of the ATR-FPA-FTIR setup to water diffusion. It also indicates the need to perform water content measurements before microprobe analyses, especially for methods with high spatial resolution (micro-FTIR, SIMS) as they might unknowingly target areas of the melt inclusions affected by enrichment or depletion of water due to electron beam.

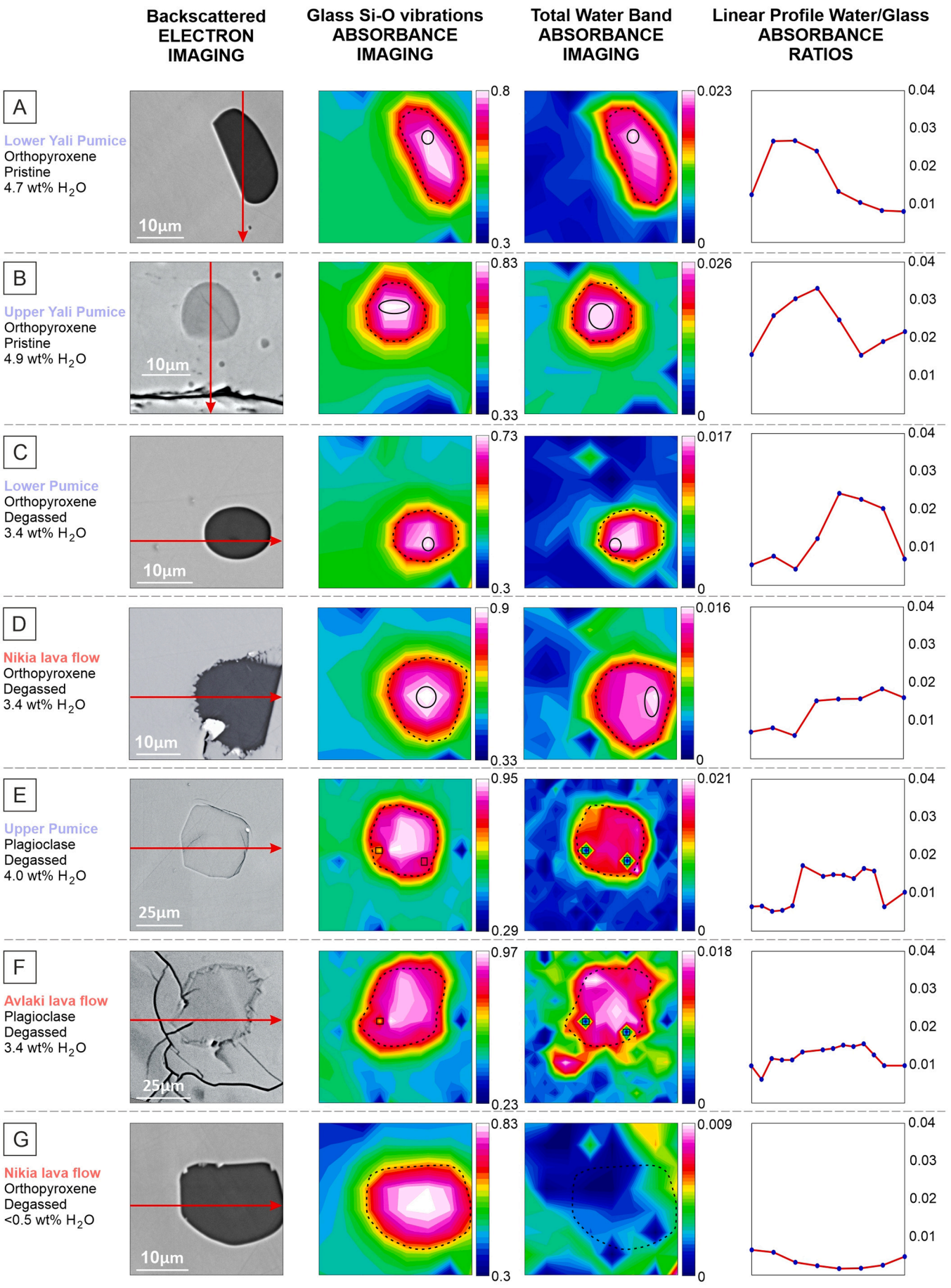

(caption on next page)

Fig. 6. Examples of spectral images used for evaluating the quality of melt inclusions. For each inclusion, an SEM-generated backscattered electron (BSE) image is compared to the structural image of the inclusion (glass Si—O vibration band). The dashed contour represents the shape of the inclusion, as seen in the BSE image. The structural images are then compared to the total water absorbance images. (A, B): The two absorbance images have the same shape, similar gradients and the location of the maximum absorbance of the images corresponds (open circles). The melt inclusions are considered to have homogenous water distribution, which is attributed to pristine water contents. (C, D): Despite having more or less the same aspect, in some melt inclusions the maximum Si—O vibration and total water absorbance signals do not spatially correspond, which suggests water diffusion. (E, F): More intense gradients in water concentration lead to a shaggy appearance of the total water absorbance images, showing areas depleted in water to various degrees. (G): In some instances, the melt inclusion appears entirely depleted of dissolved water. Cases C-G are considered to have inhomogeneous water distribution, with G actually below detection limit, which is attributed to water loss. The small squares depicted in E and F are anomalous pixels that can appear as a result of solid residue contaminating the surface of the ATR objective. The fourth column shows the ratio of total water to glass Si—O vibration absorbance, along the profiles indicated with red arrows on the BSE images. The ratios increase significantly within the melt inclusions with homogenous water distribution (A, B), while they tend to gradually flatten out and to show irregularities (C—F), or even to decrease (G) in the melt inclusions with inhomogeneous water distribution. (For interpretation of the references to colour in this figure legend, the reader is referred to the web version of this article.)

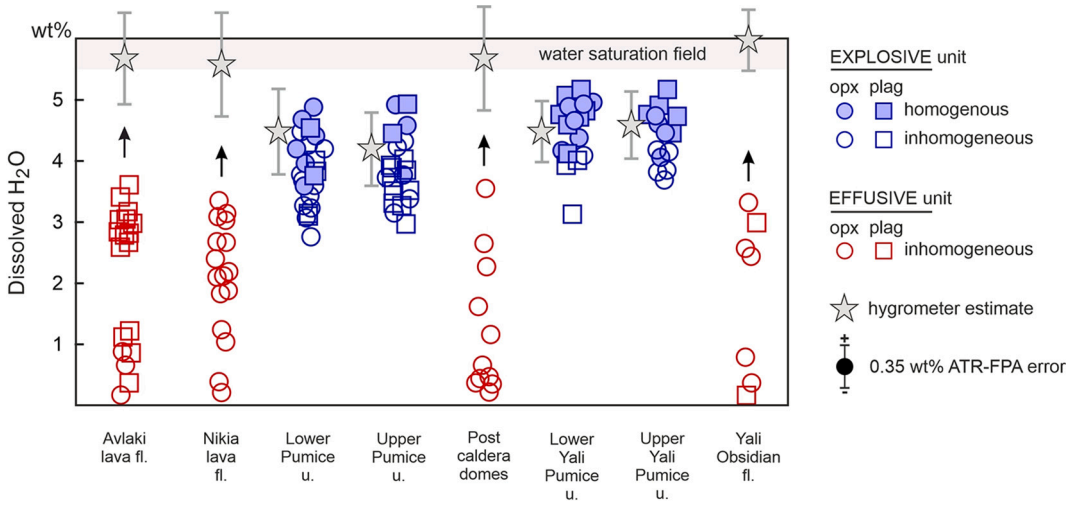

Fig. 7. Dissolved H_2O contents measured with the ATR-FPA-FTIR technique in melt inclusions from effusive (red) and explosive (blue) units. Plagioclase and orthopyroxene hosts are differentiated by using square and circle symbols, respectively. Filled symbols are melt inclusions showing homogenous water distribution, while open symbols indicate inhomogeneous melt inclusions. The data is compared to averaged plagioclase-melt hygrometry results (stars) and to the potential water saturation field (grey area), estimated by Popa et al. (2019) taking into account the rhyolitic melt compositions, storage temperatures and by varying the storage pressures (1.5–2 kbar) and CO_2 contents (100–200 ppm). The grey arrows associated to effusive events point to the higher pre-eruptive water contents expected from mineral-melt hygrometry and from the pre-eruptive water-saturated state of these magmas (Popa et al., 2021b), indicating water loss. As opposed, based on the same previously published halogen data, the melt inclusions found in the explosive units were entrapped at water-undersaturated conditions (Popa et al., 2021b). (For interpretation of the references to colour in this figure legend, the reader is referred to the web version of this article.)

Additionally, we remark that microprobe measurements, although inducing water diffusion, do not lead to leakage of water outside the inclusion. After beam exposure, the maximum water signal has a higher absorbance (0.023) when compared to the initial maximum absorbance value of the same inclusion (0.019). This is mostly an effect of water movement, from the depleted central-lower part of the melt inclusion (hit by the beam) to the upper rim, where it was enriched. However, averaging the absorbance values of the individual spectra yields the same value of ~0.019, and hence the same dissolved water content of 4.1 wt% as the initial measurement. The withstanding problem is that, although dissolved water contents can still be extracted with the ATR-FPA-FTIR even after microprobe measurements, the degassed or pristine quality of the melt inclusions cannot be assessed anymore.

When comparing our new calibration with those of Allabar and Nowak (2020) and Lowenstern and Pitcher (2013), we note that they yield comparable results in the 2–5 wt% water interval, with differences of 0 to 0.4 wt% H_2O (Fig. 9). The calibrations are surprisingly similar in this range, indicating that approximate H_2O contents could be obtained even without standards. However, the calibrations diverge at lower and higher water contents. These differences are likely due to variations in the geometry of the ATR elements and to the compositions of the glasses (peralkaline and calc-alkaline rhyolites). In terms of the ATR crystals, to render the Lowenstern and Pitcher (2013) calibration comparable to the others, we corrected for the differences in the angle of incidence (31° to 29°), following the example given in Allabar and Nowak (2020). Overall, this assessment shows that for precise quantitative analyses, each laboratory should prepare its own calibration equation, as this will be affected by differences in the ATR element of the particular machine that is being used.

4.2. Geological implications

The Nisyros and Yali melt inclusion dataset presented in Fig. 7 indicates that our ATR-FPA-FTIR calibration yields reliable and accurate quantitative results. Based on our setup and calibration, the individual pristine melt inclusions measured in explosive deposits have dissolved water contents consistent with previous plagioclase-melt hygrometry results (Popa et al., 2019). To approximate the pre-eruptive dissolved water contents of these explosive units, we average the pristine melt inclusions with >4 wt% water (considering the pristine inclusions with less water to have been entrapped at older stages of the differentiation process). The results, compared with the hygrometry data, are given in Table 1 and are generally between 4.5 and 4.7 ± 0.35 wt% H_2O, overlapping with the 4.2–4.6 ± 0.6 wt% H_2O assessed from hygrometry.

The melt inclusions analyzed in the four effusive units, by contrast, appear to be all affected by syn/post-eruptive water loss. In this case, the direct measurement of water content only gives minimal estimates of the pre-eruptive dissolved water budget of these melts, which we refer to as

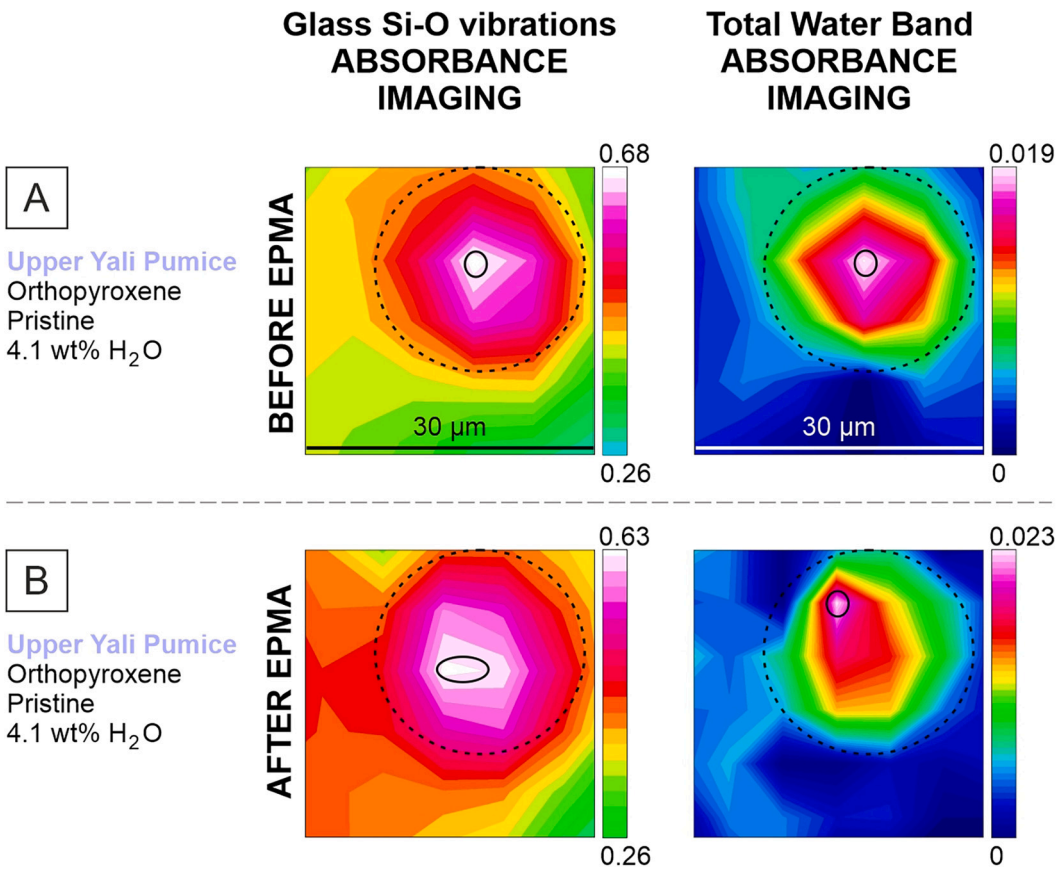

Fig. 8. Spectral images illustrating the sensitivity of the ATR-FPA method to water diffusion. The same melt inclusion, indicated by the black-dashed circle, was analyzed before and after being exposed to a microprobe electron beam (15 kV, 2 nA beam current, 5 µm defocused beam, total exposure time 80 s). The pre-EPMA total water image suggests homogenous water distribution, while the post-EPMA total water image indicates the depletion of the central and lower parts of the inclusion (subjected to the beam) and the concentration of H_2O towards the upper part.

remnant water (affected by post-entrapment processes). The maximum remnant water contents of 3.3–3.6 ± 0.35 wt% H_2O are, misleadingly, indicative of low volatile, water-undersaturated magmas. The values are well below the expected 5.6 wt% H_2O (Popa et al., 2019), and not representative of the water-saturated nature of the magmas behaving effusively at Nisyros and Yali volcanoes, as suggested by the halogen behaviour identified in the same melt inclusions and in apatite crystals (Popa et al., 2021b). This points to the fact that direct measurements of water content in effusive units will not result in accurate pre-eruptive dissolved water contents, as post-entrapment processes, especially during and after the eruption, affect the record of the melt inclusions, due to slower ascent velocities and longer cooling regimes (*e.g.* Portnyagin et al., 2008; Wright et al., 2012; Lloyd et al., 2013; Popa et al., 2019).

In our case, the most straightforward interpretation for water loss is diffusion of molecular H_2O from the melt inclusion through pre-existing dislocations or crystal cleavage (Severs et al., 2007). This process is specific for water-rich rhyolitic melts with >3 wt% dissolved water, where molecular H_2O speciation becomes important, especially during ascent-driven decompression (Silver et al., 1990; Zhang et al., 1991; Rangel et al., 2018). The slow cooling regime at surface pressure also favors molecular water speciation at the detriment of OH (Silver et al., 1990), and can additionally deplete the water content of a melt inclusion. As opposed to this, the presence of pristine melt inclusion populations in explosive deposits can be attributed to faster ascent velocities (*e.g.* Gonnermann and Manga, 2007) and to rapid quenching at the surface, which inhibit post-emplacement speciation to molecular water (Silver et al., 1990). However, we note that even in explosive deposits, a large population of the melt inclusions can be affected by gas loss, especially in thick units subjected to longer cooling timescales, as those generated by caldera-collapse events. In this latter case, based on the Nisyros caldera-collapse deposits, 65–75% of the melt inclusions have experienced post-emplacement water loss, as opposed to only 20–35% in the smaller-scale (and submarine) explosions of Yali volcano. In the absence of quality evaluations that allow the filtering out of degassed inclusions, this can severely impact interpretations and further calculations based on the determined pre-eruptive H_2O contents.

5. Conclusions

The calibration for the ATR-FPA-FTIR technique used for estimating the total dissolved water content of rhyolitic glasses performs well. It offers good reproducibility and accuracy when used on standards, with an uncertainty of ±0.35 wt%. When the technique is applied to melt inclusions unaffected by gas loss, it yields similar results with plagioclase-melt hygrometry: 4.5–4.7 ± 0.35 wt% H_2O compared to 4.2–4.6 ± 0.6 wt% H_2O, respectively, for our set of samples from Nisyros and Yali volcanoes. Due to the particularities of our FTIR setup, which requires opening the sample chamber prior to each analysis, we prefer using the global calibration equation, which accounts for a range of variations induced by changing atmospheric conditions and air turbulence within the chamber. Full automation of the ATR measurements without opening the sample chamber could preserve constant atmospheric conditions throughout the daily analytical sessions, in which case users could opt for daily calibrations instead, which may reduce the uncertainty.

The high-resolution imaging of water distribution is highly sensitive to H_2O diffusion. It can be combined with the structural imaging of the glass (Si—O vibrations), providing a means of assessing the reliability of

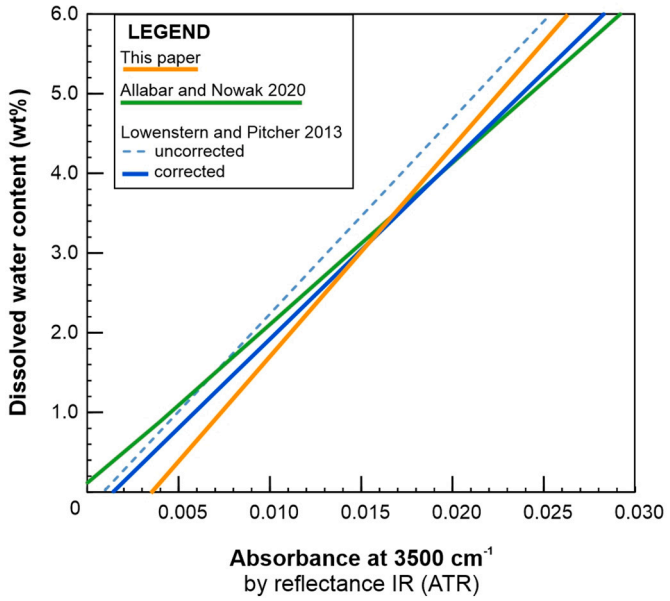

Fig. 9. Comparison of ATR-FTIR calibration lines from this study (Ge crystal, incidence angles of 21.5° to 37°, 2.6 N force, calc-alkaline rhyolites), Allabar and Nowak (2020) (Ge crystal, incidence angles of 21.5° to 37°, 4.4 N force, peralkaline rhyolites) and Lowenstern and Pitcher (2013) (Ge crystal, incidence angle of 31°, calc-alkaline rhyolites). For the latter, we corrected the absorbance values for the different incidence angle of the ATR objective, and plot both the corrected and uncorrected calibration lines.

Table 1
Comparative averaged results of dissolved water contents derived by ATR-FPA-FTIR (this paper) and plagioclase-melt hygrometry (Popa et al., 2019), for the explosive units of Nisyros and Yali volcanoes. The Waters and Lange (2015) hygrometer was employed, using as input plagioclase rims and groundmass glass compositions, along with storage temperatures determined by amphibole-plagioclase thermometry (Holland and Blundy, 1994).

Unit	Volcano	Eruptive style	ATR-FPA wt% water	Hygrometry wt% water
Lower Pumice	Nisyros	explosive	4.5 ± 0.35	4.5 ± 0.7
Upper Pumice	Nisyros	explosive	4.7 ± 0.35	4.2 ± 0.6
Lower Pumice	Yali	explosive	4.7 ± 0.35	4.5 ± 0.5
Upper Pumice	Yali	explosive	4.7 ± 0.35	4.6 ± 0.55

melt inclusion volatile records. This makes it possible to evaluate whether melt inclusions have lost water or not, which is key to properly interpreting water data derived from direct measurements. Hence, it offers a solution to one of the main problems when working with melt inclusions. Application of this calibration and FTIR setup opens up new possibilities to measure and interpret the volatile records of melt inclusions and their host magmas, as well as to aid experimental petrology studies in assessing and quantifying degassing.

Directly comparing the dissolved total water contents measured in effusive and explosive deposits is biased by the different cooling and degassing regimes. The bias is evident from the water distribution images, which indicate consistent, considerable and variable water loss from melt inclusions preserved in lava samples. A key conclusion is that direct measurements of water content in melt inclusions preserved in effusive units will not yield accurate pre-eruptive volatile budgets, but only minimal estimates affected by *syn*- and post-eruptive processes. Mineral-melt hygrometers should therefore be the preferred option to determine dissolved water contents for lavas (assuming fresh glass). On the other hand, for explosive deposits, direct measurements can yield water contents that are representative of the magmatic reservoir conditions. However, even these are usually affected by variable degrees of post-emplacement water loss, depending potentially on the thickness and cooling regime of the tephra deposits. As our data show, in the Nisyros-Yali caldera-forming eruptions, up to 75% of the melt inclusions are affected by water loss, while even in smaller explosive deposits up to 35% of inclusions can be degassed. For an accurate determination of dissolved water contents, the pristine or degassed nature of these inclusions has to be appraised qualitatively, which will allow for the precise identification of the representative melt inclusion population. Also, derived from this, it appears that determining vertical extents and depths of magmatic reservoirs based on melt inclusion records without such a quality assessment can be inaccurate, potentially leading to shallower storage depths and greater thicknesses than in reality, as degassed melt inclusions will be unintentionally considered in the calculations.

Overall, the combination of ATR-FPA-FTIR and mineral-melt hygrometry is a powerful tool for understanding the volatile evolution of a dynamic magmatic system, and can be further coupled to other techniques, such as measuring halogens and OH groups in minerals like apatite (Stock et al., 2018; Li and Hermann, 2017; Li and Costa, 2020; Popa et al., 2021b; Humphreys et al., 2021; Hammerli et al., 2021). ATR-FPA-FTIR and mineral-melt hygrometry should yield similar water contents for explosive units. For effusive units, the direct melt inclusion measurements will likely yield the lower limit of possible water content, while the hygrometry-derived water concentrations will provide an upper, more accurate estimate.

With proper calibration standards, this method can be adapted to estimate water contents and to image the water distribution in melt inclusions from volatile poorer, mafic melts, such as basalts. The main challenge to overcome is improving the detection limit, by dealing with the low signal-to-noise ratio characteristic of the total water band at low absorbance intensities. This could be addressed by using a fully automated ATR-FPA-FTIR setup combined with increasing the scans-per-frame during the measurement routine. This should also increase the precision of the method, which can be further augmented by employing daily calibration equations.

Ackowledgements

This work was supported by the Swiss National Science Foundation grants No. 200021_178928 to O.B. and No. 200021_169062 to P.T and J. H. We thank Prof. Peter Ulmer for providing the calibration glasses and Ewa Krymarys for assistance with the Raman measurements. We would like to thank Dr. Jake Lowenstern, Dr. Margaret Hartley and an anonymous reviewer for their constructive feedback on this manuscript, and Prof. Balz Kamber for editorial handling.

Declaration of Competing Interest

The authors declare that they have no known competing financial interests or personal relationships that could have appeared to influence the work reported in this paper.

Data availability

Data is attached as supplementary files.

Appendix A. Supplementary data

Supplementary data to this article can be found online at https://doi.org/10.1016/j.chemgeo.2022.121217.

References

Allabar, A., Nowak, M., 2020. High spatial resolution analysis of H_2O in silicate glass using attenuated total reflection FTIR spectroscopy coupled with a focal plane array detector. Chem. Geol. 556, 119883.

Allabar, A., Dobson, K.J., Bauer, C.C., Nowak, M., 2020. Vesicle shrinkage in hydrous phonolitic melt during cooling. Contrib. Mineral. Petrol. 175, 21.
Allaz, J.M., Popa, R.-G., Reusser, E., Martin, L., 2019. Electron microprobe analysis of minor and trace elements in beam sensitive materials: how far can we go? Microsc. Microanal. 25, 2312–2313.
Ardia, P., Giordano, D., Schmidt, M.W., 2008. A model for the viscosity of rhyolite as a function of H_2O-content and pressure: a calibration based on centrifuge piston cylinder experiments. Geochim. Cosmochim. Acta 72, 6103–6123.
Bachmann, O., Wallace, P.J., Bourquin, J., 2010. The melt inclusion record from the rhyolitic Kos Plateau Tuff (Aegean Arc). Contrib. Mineral. Petrol. 159, 187–202.
Bachmann, O., Allen, S.R., Bouvet de Maisonneuve, C., 2019. The Kos-Nisyros-Yali volcanic field. Elements 15, 191–196.
Bacon, C.R., 1992. Water, CO2, Cl, and F in melt inclusions in phenocrysts from three Holocene explosive eruptions, Crater Lake, Oregon. Am. Mineral. 77, 1021–1030.
Balcone-Boissard, H., Boudon, G., Blundy, J.D., Martel, C., Brooker, R.A., Deloule, E., Solaro, C., Matjuschkin, V., 2018. Deep pre-eruptive storage of silicic magmas feeding Plinian and dome-forming eruptions of central and northern Dominica (Lesser Antilles) inferred from volatile contents of melt inclusions. Contrib. Mineral. Petrol. 173, 101.
Behrens, H., Nowak, M., 2003. Quantification of H_2O speciation in silicate glasses and melts by IR Spectroscopy – in situ versus quench techniques. Phase Transit. 76, 45–61.
Blundy, J., Cashman, K., 2005. Rapid decompression-driven crystallization recorded by melt inclusions from Mount St. Helens volcano. Geology 33, 793–796.
Cassidy, M., Castro, J.M., Helo, C., Troll, V.R., Deegan, F.M., Muir, D., Neave, D.A., Mueller, S.P., 2016. Volatile dilution during magma injections and implications for volcano explosivity. Geology 44, 1027–1030.
Cassidy, M., Manga, M., Cashman, K., Bachmann, O., 2018. Controls on explosive-effusive volcanic eruption styles. Nat. Commun. 9, 2839.
Chabiron, A., Pironon, J., Massare, D., 2004. Characterization of water in synthetic rhyolitic glasses and natural melt inclusions by Raman spectroscopy. Contrib. Mineral. Petrol. 146, 485–492.
Compton, S.V., Compton, D.A.C., 1993. Optimization of data recorded by internal reflectance spectroscopy. In: Coleman, P.B. (Ed.), Practical Sampling Techniques for Infrared Analysis 55–92. CRC Press, p. 301.
Degruyter, W., Huber, C., Bachmann, O., Cooper, K.M., Kent, A.J.R., 2017. Influence of exsolved volatiles on reheating silicic magmas by recharge and consequences for eruptive style at Volcan Quizapu (Chile). Geochem. Geophys. Geosyst. https://doi.org/10.1002/2017GC007219.
Deloule, E., Paillat, O., Pichavant, M., Scaillet, B., 1995. Ion microprobe determination of water in silicate glasses: methods and applications. Chem. Geol. 125, 19–28.
Devine, J.D., Gardner, J.E., Brack, H.P., Layne, G.D., Rutherford, M.J., 1995. Comparison of microanalytical methods for estimating H2O contents of silicic volcanic glasses. Am. Mineral. 80, 319–328.
Di Genova, D., Sicola, S., Romano, C., Vona, A., Fanara, S., Spina, L., 2017. Effect of iron and nanolites on Raman spectra of volcanic glasses: a reassessment of existing strategies to estimate the water content. Chem. Geol. 475, 76–86.
Donovan, A., Blundy, J., Oppenheimer, C., Buisman, I., 2018. The 2011 eruption of Nabro volcano, Eritrea: perspectives on magmatic processes from melt inclusions. Contrib. Mineral. Petrol. 173, 1.
Edmonds, M., Woods, A.W., 2018. Exsolved volatiles in magma reservoirs. J. Volcanol. Geotherm. Res. 368, 13–30.
Esposito, R., Lamadrid, H.M., Redi, D., Steele-MacInnis, M., Bodnar, R.J., Manning, C.E., De Vivo, B., Cannatelli, C., Lina, A., 2016. Detection of liquid H_2O in vapor bubbles in reheated melt inclusions: implications for magmatic fluid composition and volatile budgets of magmas? Am. Mineral. 101, 1691–1695.
Ewing, A.V., Clarke, G.S., Kazarian, S.G., 2016. Attenuated total reflection-Fourier transform infrared spectroscopic imaging of pharmaceuticals in microfluidic devices. Biomicrofluidics 10, 024125. https://doi.org/10.1063/1.4946867.
Gaetani, G.A., O'Leary, J.A., Shimizu, N., Bucholz, C.E., Newville, M., 2012. Rapid reequilibration of H_2O and oxygen fugacity in olivine-hosted melt inclusions. Geology 40, 915–918.
Gaillard, F., Schmidt, B., Mackwell, S., McCammon, C., 2003. Rate of hydrogen–iron redox exchange in silicate melts and glasses. Geochim. Cosmochim. Acta 67, 2427–2441.
Gonnermann, H.M., Manga, M., 2007. The fluid mechanics inside a volcano. Annu. Rev. Fluid Mech. 39, 321–356.
Hammerli, J., Hermann, J., Tollan, P., Naab, F., 2021. Measuring in situ CO_2 and H_2O in apatite via ATR-FTIR. Contrib. Mineral. Petrol. 176, 105.
Harms, E., Schmincke, H.-U., 2000. Volatile composition of the phonolitic Laacher See magma (12,900 yr BP): implications for syn-eruptive degassing of S, F, Cl and H_2O. Contrib. Mineral. Petrol. 138, 84–98.
Heinrich, C.A., Candela, P.A., 2014. Fluids and ore formation in the earth's crust. Treat. Geochem. 2nd edn 13, 1–28.
Hervig, R.L., Dunbar, N., Westrich, H.R., Kyle, P.R., 1989. Pre-eruptive water content of rhyolitic magmas as determined by ion microscope analyses of melt inclusions in phenocrysts. J. Volcanol. Geotherm. Res. 36, 293–302.
Hess, K.-U., Dingwell, D.B., 1996. Viscosities of hydrous leucogranitic melts: a non-Arrhenian model. Am. Mineral. 81, 1297–1300.
Holland, T., Blundy, J., 1994. Non-ideal interactions in calcic amphiboles and their bearing on amphibole-plagioclase thermometry. Contrib. Mineral. Petrol. 116, 433–447.
Humphreys, M.C.S., Kearns, S.L., Blundy, J.D., 2006. SIMS investigation of electron-beam damage to hydrous, rhyolitic glasses: Implications for melt inclusion analysis. Am. Mineral. 91, 667–679.
Humphreys, M.C.S., Menand, T., Blundy, J.D., Klimm, K., 2008. Magma ascent rates in explosive eruptions: Constraints from H2O diffusion in melt inclusions. Earth Planet. Sci. Lett. 270, 25–40.
Humphreys, M.C.S., Smith, V.C., Comans, J.P., Riker, J.M., Stock, M.J., de Hoog, J.C.M., Brooker, R.A., 2021. Rapid pre-eruptive mush reorganisation and atmospheric volatile emissions from the 12.9 ka Laacher See eruption, determined using apatite. Earth Planet. Sci. Lett. 576, 117198.
Huppert, H.E., Woods, A.W., 2002. The role of volatiles in magma chamber dynamics. Nature 420.
Kazarian, S.G., Chan, K.L.A., 2006. Applications of ATR-FTIR spectroscopic imaging to biomedical samples. Biochim. Biophys. Acta Biomembr. 1758, 858–867.
Kazarian, S.G., Chan, L.A., 2013. ATR-FTIR spectroscopic imaging: recent advances and applications to biological systems. Analyst 138, 1940–1951.
Kent, A.J.R., 2008. Melt inclusions in basaltic and related volcanic rocks, in Putirka KD, Tepley FJ, eds., Minerals, inclusions and volcanic processes. Rev. Mineral. Geochem. 69, 273–331.
Kilgour, G., Blundy, J., Cashman, K., Mader, H., 2013. Small volume andesite magmas and melt-mush interactions at Ruapehu, New Zealand: evidence from melt inclusions. Contrib. Mineral. Petrol. 166, 371–392.
Li, W., Costa, F., 2020. A thermodynamic model for F-Cl-OH partitioning between silicate melts and apatite including non-ideal mixing with application to constraining melt volatile budgets. Geochim. Cosmochim. Acta 269, 203–222.
Li, H., Hermann, J., 2017. Chlorine and fluorine partitioning between apatite and sediment melt at 2.5 GPa, 800 °C: a new experimentally derived thermodynamic model. Am. Mineral. 102, 580–594.
Liu, Y., Anderson, A.T., Wilson, C.J.N., Davis, A.M., Steele, I.M., 2006. Mixing and differentiation in the Oruanui rhyolitic magma, Taupo, New Zealand: evidence from volatiles and trace elements in melt inclusions. Contrib. Mineral. Petrol. 151, 71–87.
Lloyd, A.S., Plank, T., Ruprecht, P., Hauri, E.H., Rose, W., 2013. Volatile loss from melt inclusions in pyroclasts of differing sizes. Contrib. Mineral. Petrol. 165, 129–153.
Lowenstern, J.B., Pitcher, B.W., 2013. Analysis of H2O in silicate glass using attenuated total reflectance (ATR) micro-FTIR spectroscopy. Am. Mineral. 98, 1660–1668.
McIntosh, I.M., Llewellin, E.W., Humphreys, M.C.S., Nichols, A.R.L., Burgisser, A., Schipper, C.I., Larsen, J.F., 2014. Distribution of dissolved water in magmatic glass records growth and resorption of bubbles. Earth Planet. Sci. Lett. 401, 1–11.
Mirabella, F.M., 1983. Strength of interaction and penetration of infrared radiation for polymer films in internal reflection spectroscopy. J. Polym. Sci. Polym. Phys. Ed. 21, 2403–2417.
Moore, L.R., Gazel, E., Tuohy, R., Lloyd, A.S., Esposito, R., Steele-MacInnis, M., Hauri, E. H., Wallace, P.J., Plank, T., Bodnar, R.J., 2015. Bubbles matter: an assessment of the contribution of vapor bubbles to melt inclusion volatile budgets. Am. Mineral. 100, 806–823.
Morgan, G.B., London, D., 1996. Optimizing the electron microprobe analysis of hydrous alkali aluminosilicate glasses. Am. Mineral. 81, 1176–1185.
Pistone, M., Caricchi, L., Ulmer, P., Reusser, E., Ardia, P., 2013. Rheology of volatile-bearing crystal mushes: Mobilization vs. viscous death. Chem. Geol. 345, 16–39.
Pistone, M., Arzilli, F., Dobson, K.J., Cordonnier, B., Reusser, E., Ulmer, P., Marone, F., Whittington, A.G., Mancini, L., Fife, J.L., Blundy, J.D., 2015. Gas-driven filter pressing in magmas: Insights into in-situ melt segregation from crystal mushes. Geology 43, 699–702.
Popa, R.-G., Bachmann, O., Ellis, B.S., Degruyter, W., Tollan, P., Kyriakopoulos, K., 2019. A connection between magma chamber processes and eruptive styles revealed at Nisyros-Yali volcano (Greece). J. Volcanol. Geotherm. Res. 387, 106666.
Popa, R.-G., Guillong, M., Bachmann, O., Szymanowski, D., Ellis, B., 2020. U-Th zircon dating reveals a correlation between eruptive styles and repose periods at the Nisyros-Yali volcanic area, Greece. Chem. Geol. 555, 119830.
Popa, R.-G., Bachmann, O., Huber, C., 2021a. Explosive or effusive style of volcanic eruption determined by magma storage conditions. Nat. Geosci. 14, 781–786.
Popa, R.-G., Tollan, P., Bachmann, O., Schenker, V., Ellis, B., Allaz, J.M., 2021b. Water exsolution in the magma chamber favors effusive eruptions: Application of Cl-F partitioning behavior at the Nisyros-Yali volcanic area. Chem. Geol. 570, 120170.
Portnyagin, M., Almeev, R., Matveev, S., Holtz, F., 2008. Experimental evidence for rapid water exchange between melt inclusions in olivine and host magma. Earth Planet. Sci. Lett. 272, 541–552.
Rangel, E., Arce, J.L., Macias, J.L., 2018. Storage conditions of the ~29 ka rhyolitic Guangoche White Pumice Sequence, Los Azufres Volcanic Field, Central Mexico. J. Volcanol. Geotherm. Res. 358, 132–148.
Reubi, O., Blundy, J., Varley, N.R., 2013. Volatiles contents, degassing, and crystallisation of intermediate magmas at Volcán de Colima, Mexico: the role of H_2O, CO_2, and diffusive reequilibration of melt inclusions. Contrib. Mineral. Petrol. 165, 1087–1106.
Schneider, C.A., Rasband, W.S., Eliceiri, K.W., 2012. NIH image to ImageJ: 25 years of image analysis. Nat. Methods 9, 671–675.
Severs, M.J., Azbej, T., Thomas, J.B., Mandeville, C.W., Bodnar, R.J., 2007. Experimental determination of H_2O loss from melt inclusions during laboratory heating: evidence from Raman spectroscopy. Chem. Geol. 237, 358–371.
Sillitoe, R.H., 2010. Porphyry Copper Systems. Econ. Geol. 105, 3–41.
Silver, L.A., Ihinger, P.D., Stolper, E., 1990. The influence of bulk composition on the speciation of water in silicate glasses. Contrib. Mineral. Petrol. 104, 142–162.
Sisson, T.W., Bacon, C.R., 1999. Gas-driven filter pressing in magmas. Geology 27, 613–616.
Stock, M.J., Humphreys, M.C.S., Smith, V.C., Isaia, R., Brooker, R.A., Pyle, D.M., 2018. Tracking volatile behaviour in sub-volcanic plumbing systems using apatite and glass: insights into pre-eruptive processes at Campi Flegrei, Italy. J. Petrol. 59, 2463–2492.

Stolper, E., 1982. Water in silicate glasses: an infrared spectroscopic study. Contrib. Mineral. Petrol. 81, 1–17.
Thomas, R., 2000. Determination of water contents of granite melt inclusions by confocal laser Raman microprobe spectroscopy. Am. Mineral. 85, 868–872.
Tollan, P., Ellis, B., Troch, J., Neukampf, J., 2019. Assessing magmatic volatile equilibria through FTIR spectroscopy of unexposed melt inclusions and their host quartz: a new technique and application to the Mesa Falls Tuff, Yellowstone. Contribut. Mineral. Petrol. 174, 24.
Vigneresse, J.-L., Truche, L., Richard, A., 2019. How do metals escape from magmas to form porphyry-type ore deposits? Ore Geol. Rev. 105, 310–336.
Wallace, P.J., 2005. Volatiles in subduction zone magmas: concentrations and fluxes based on melt inclusion and volcanic gas data. J. Volcanol. Geotherm. Res. 140, 217–240.
Wallace, P.J., Gerlach, T.M., 1994. Magmatic Vapor Source for Sulfur Dioxide Released during Volcanic Eruptions: evidence from Mount Pinatubo. Science 265, 497–499.
Wallace, P.J., Anderson Jr., A.T., Davis, A.M., 1999. Gradients in H2O, CO2, and exsolved gas in a large-volume silicic magma system: Interpreting the record preserved in melt inclusions from the Bishop Tuff. J. Geophys. Res. 104, 20097–21122.
Waters, L.E., Lange, R.A., 2015. An updated calibration of the plagioclase-liquid hygrometer-thermometer applicable to basalts through rhyolites. Am. Mineral. 100, 2172–2184.
Webster, J.D., Rebbert, C.R., 2001. The geochemical signature of fluid-saturated magma determined from silicate meltinclusions in Ascension Island granite xenoliths. Geochim. Cosmochim. Acta 65, 123–136.
Wright, H.M., Bacon, C.R., Vazquez, J.A., Sisson, T.W., 2012. Sixty thousand years of magmatic volatile history before the caldera-forming eruption of Mount Mazama, Crater Lake, Oregon. Contrib. Mineral. Petrol. 164, 1027–1052.
Zajacs, Z., Halter, W., Malfait, W.J., Bachmann, O., Bodnar, R.J., Hirschmann, M.M., Mandeville, C.W., Morizet, Y., Muntener, O., Ulmer, P., Webster, J.D., 2005. A composition-independent quantitative determination of the water content in silicate glasses and silicate melt inclusions by confocal Raman spectroscopy. Contrib. Mineral. Petrol. 150, 631–642.
Zhang, Y., Stolper, E.M., Wasserburg, G.J., 1991. Diffusion of water in rhyolitic glasses. Geochim. Cosmochim. Acta 55, 441–456.
Zhang, Y., Belcher, R., Ihinger, P.D., Wang, L., Xu, Z., Newman, S., 1997. New calibration of infrared measurement of water in rhyolitic glasses. Geochim. Cosmochim. Acta 61, 3089–3100.